Journal of ASTM International, Vol. 6, No. 2
Paper ID JAI101849
Available online at www.astm.org

Noam Lior[1] *and Dimitrios Papadopoulos*[2]

Gas-Cooling of Multiple Short Inline Disks in Flow Along Their Axis

ABSTRACT: To learn about cooling of gas quenched batches, this paper reports on numerical predictions of local and average convective heat transfer coefficients, and overall pressure drops, on batches of five axially aligned, constant temperature, short cylindrical disks (25 cm diameter, 5 cm thickness) with and without a concentric hole, with interdisk spacings of 5–20 cm, in axial turbulent flows of 20 bar nitrogen gas at inlet speeds from 10 m/s to 100 m/s, corresponding to Reynolds numbers (Re) between 3.27×10^6 and 32.7×10^6. The heat transfer coefficients along the disk surfaces vary strongly up to a worse case of two orders of magnitude for the upstream disk. This nonuniformity is much lower for the disks downstream, especially after spacing is increased beyond 0.1 m. As expected, the upstream disk exhibited rather different heat transfer coefficients than the ones downstream, the magnitude of the heat transfer coefficient and its uniformity increased with the interdisk spacing, and varied by a factor of about 4–5 along the surfaces. The average heat transfer coefficient (Nusselt number, Nu) on the disks increased approximately with Reynolds number as $\mathrm{Re}^{0.85}$. Re did not have much influence on the nonuniformity of Nu on the disk surfaces. The overall pressure drop along the flow increases with the interdisk spacing, rising by about 60 % as the spacing is increased from 0.05 m to 0.20 m. The presence of a hole increases the heat transfer coefficient in all cases. Some suggestions for reducing the heat transfer coefficient nonuniformity are made.

KEYWORDS: quenching, gas quenching, quenching simulation, quenching uniformity, convective heat transfer

Nomenclature

a = interdisk spacing, m
C_μ = coefficient in the k-ε model, $C_\mu=0.09$
d_i = hole diameter, m
d_o = disk outside diameter, m
h = convective heat transfer coefficient, $h\equiv-(k\nabla T/(T_s-T_i))_{\text{at disk surface}}$
I = turbulence intensity, $I=v/V_i$
k = thermal conductivity of the gas, W/(m·K)
k_t = turbulence kinetic energy
Nu = local Nusselt number, $\equiv hd_o/k$
r = radial direction
Re = Reynolds number $\equiv V_i d_o/\nu$
T = temperature, °C
T_i = gas upstream temperature, °C
T_s = temperature of disk surface, °C
u^* = $C_\mu^{1/4}k_t^{1/2}$
v = local turbulent fluctuation velocity, m/s
V_i = upstream velocity, m/s
y^+ = $(u^*\Delta n/4)/\mu$

Greek

Δn = normal distance between the wall and the first computational grid point away from the wall
μ = dynamic viscosity, $(\mathrm{N}\cdot\mathrm{s})/\mathrm{m}^2$
ν = kinematic viscosity, m^2/s

Manuscript received April 30, 2008; accepted for publication November 25, 2008; published online December 2008.
[1] Department of Mechanical Engineering and Applied Mechanics, University of Pennsylvania, Philadelphia, PA 19104-6315, E-mail: lior@seas.upenn.edu
[2] Faxénlaboratoriet, KTH, SE-100 44 Stockholm, Sweden.

Introduction

The use of gas instead of liquid as quenchant has environmental, product quality, process control, safety, and economic advantages [1], and its improvement is under intensive study at the Faxén Laboratory of the Royal Institute of Technology, Sweden [2–10] and elsewhere [11]. The primary effort is focused on finding ways to generate sufficiently high heat transfer coefficients, and to produce cooling which results in minimal distortions and most uniform mechanical properties of the quenched parts. Of particular interest and complexity is the heat transfer when batches of parts are being quenched in the same gas stream, since each part affects the flow around the others in the batch, and at worst blocks the flow from reaching some of them. A study was published recently [12] of different, practically relevant quench load configurations: oblong parts that are arranged in the main flow direction, parts with a high grade of cross-sectional

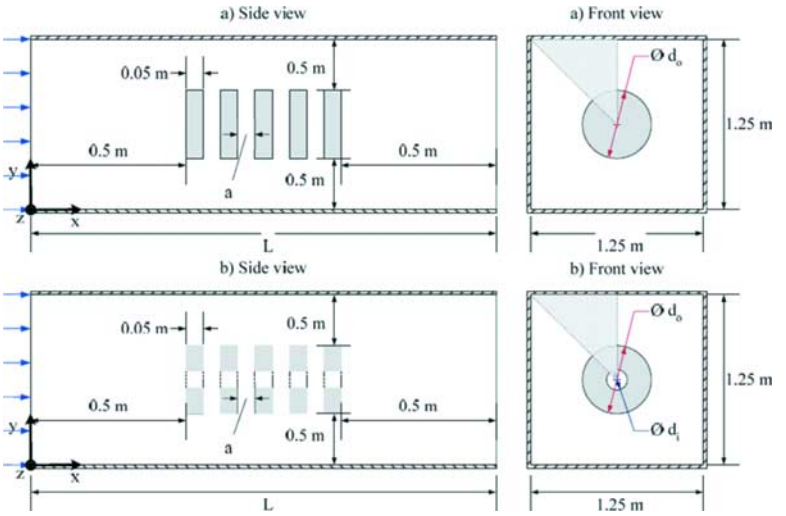

FIG. 1—*Schematic of axial flow. (a) Solid disks. (b) Disks with concentric hole. The gray shaded part illustrates the reduced computational domains where symmetry surfaces are used. Computations were made for interdisk spacings a of 0.05, 0.10, 0.15, and 0.20 m.* $d_o = 0.25$ *m,* $d_i = 0.15$. *L is the length (axial) of the computational domain (say, quench chamber) with distances of 0.5 m from the inlet to the first disk and the exit to the last disk.*

TABLE 1—*The computer runs performed.* $d_o = 0.25$ *m,* $d_i = 0.15$ *m,* $T_i = 20°C$, $p_i = 20$ *bar.*

Disk type	*a*, cm	V_i, m/s
Solid	5, 10 15, and 20	20
With hole	5, 10 15, and 20	20
With hole	5	10 and 100

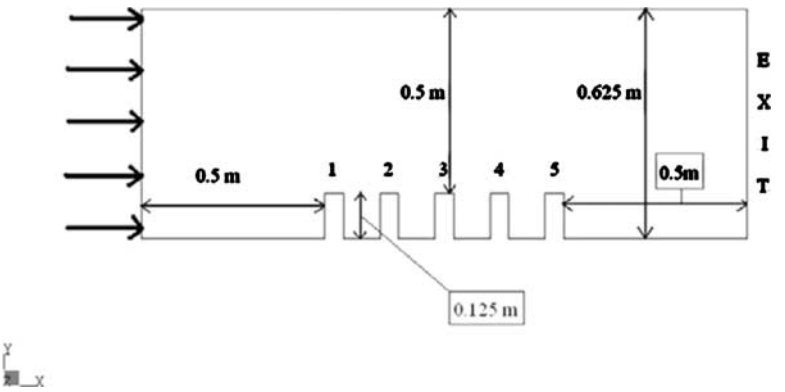

FIG. 2—*Schematic drawing for the top half of the computational domain and the disks in axial flow.*

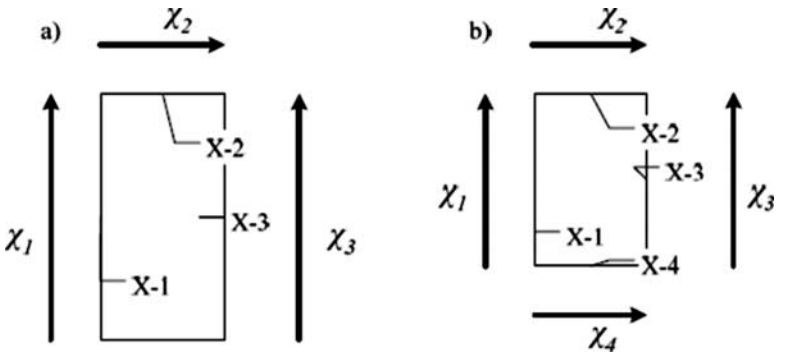

FIG. 3—*A description of the directions on each disk, used in the following plot presentations and discussion. (a) Solid disks. (b)Disks with concentric hole. The flow direction is from left to right. X-y denotes the disk number, where* $X=1$ *is the most upstream disk, with* $X=2,3,4,5$ *sequentially following in the flow direction, and y is the surface number on the disk.* χ *is the dimensionless coordinate along each surface, and equals the distance normalized by the surface length of that surface, with the arrow showing the direction in which the graphs of Figs. 5–7, 12–15, and 17–20 are plotted.*

blocking that are in several planes, and the distinction between aligned and misaligned setups of the parts. Experimental and numerical results of the gas flow distribution, the quenching intensity, and the resulting distribution of the heat transfer of the parts arranged in the different load setups were described.

The general objective of this study (a much more limited and shorter version was presented in [13]) is to determine the effects of charge configuration and of the turbulent, high-upstream-turbulence-intensity

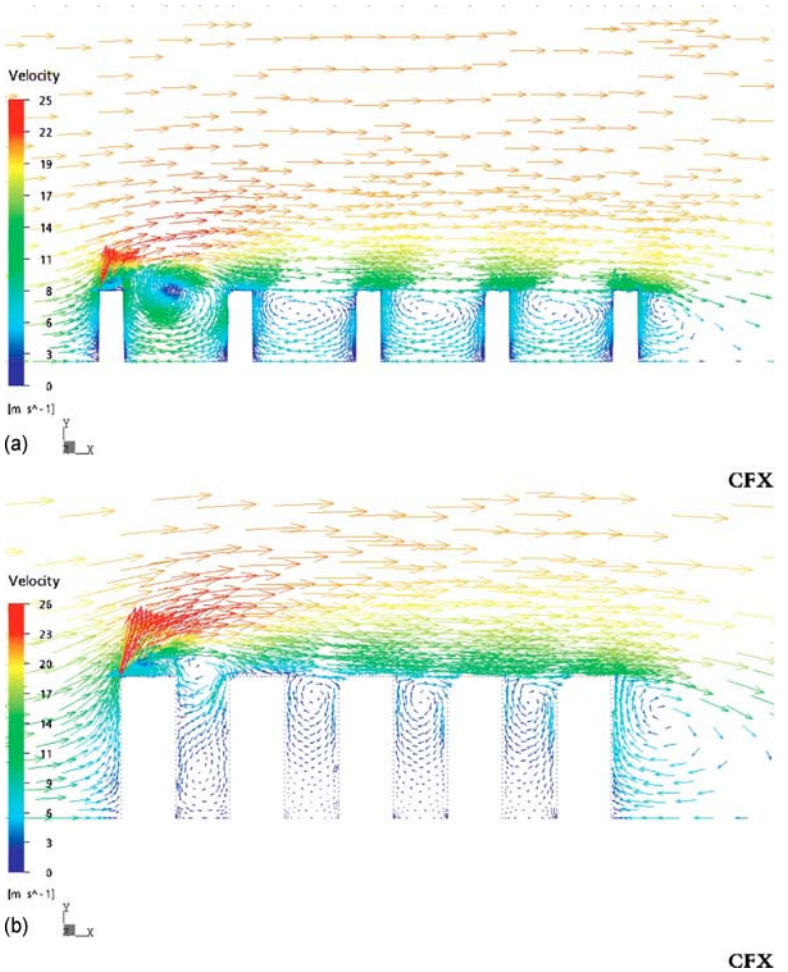

FIG. 4—*The computed velocity field for solid disks at interdisk spacings (a) of (a) 0.05 m and (b) 0.20 m.* $V_i=20\ m/s$ $(Re=6.54\times10^6)$.

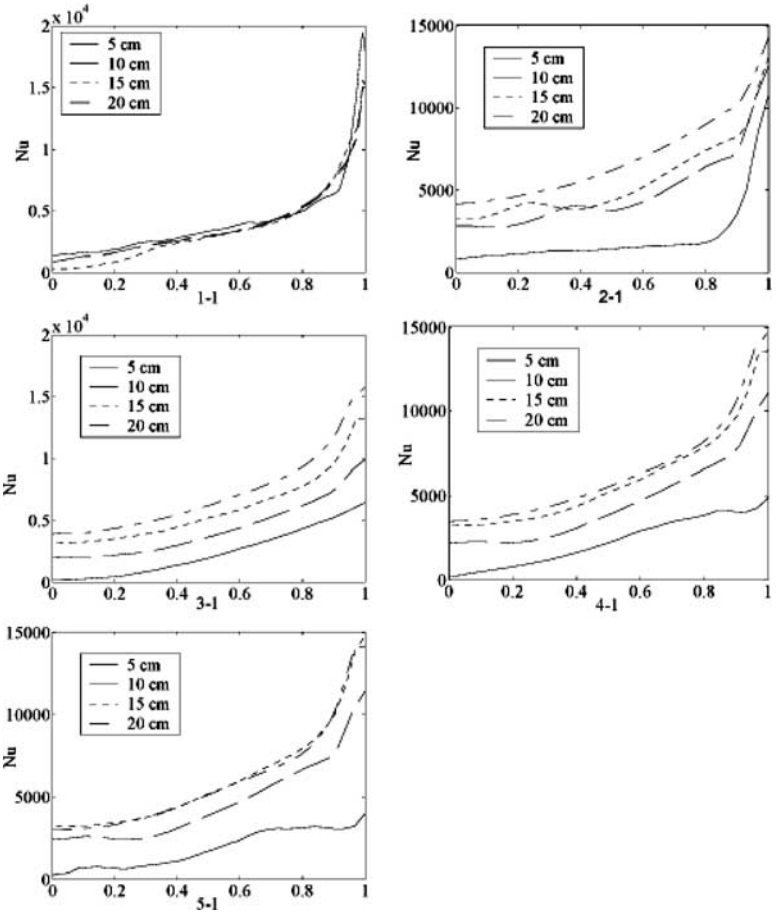

FIG. 5—*The computed Nusselt number (Nu) variation over the frontal surface of each disk, for all inter-disk spacings. The abscissas are the dimensionless coordinate* χ_1. $V_i = 20$ *m/s* ($Re = 6.54 \times 10^6$).

flow Reynolds number (Re) on the magnitude and distribution of convective heat transfer coefficients h (in the form of the Nusselt number Nu) on charges composed of five axially aligned cylindrical disks without ("solid") and with concentric holes and subjected to flow directed in the direction parallel to the disk axis. The information is used to find ways for improving the cooling uniformity.

The Considered Geometry and Quenchant

The studied configuration consists of five cylindrical disks, either solid or having a concentric hole, as shown in Fig. 1. The domain dimensions were chosen by numerical experiments to be large enough so that its effects on the flow field become negligible. The gray shaded part in Fig. 1(*b*) illustrates the reduced computational domains where symmetry surfaces are used.

Table 1 summarizes the conditions for the performed computations. The gas used in this study is nitrogen at a inlet temperature of 20°C and pressure of 20 bar (2 MPa), which is a typical pressure in gas quenching, where $\rho = 23.6$ kg/m^3, $\nu = 7.67 \times 10^{-7}$ m^2/s, and the upstream velocities used are 10, 20, and 100 m/s, corresponding to Reynolds numbers from 3.27×10^6 to 32.7×10^6. Velocities of 10 m/s and 20 m/s are typical to practical gas quenching, while 100 m/s was chosen just to examine upper limits and trends, and we note that it is still less than 1/3 of the speed of sound and thus does not indtroduce compressibility effects or flow choking.

The Computation Scope and Method

The heat transfer coefficients are computed by the finite volume simulation code software CFX-5.5 [14]. The code solves the transient three-dimensional Navier–Stokes and energy equations, together with the k-ε turbulence model. This is the most widely used turbulence model, and while there are more advanced

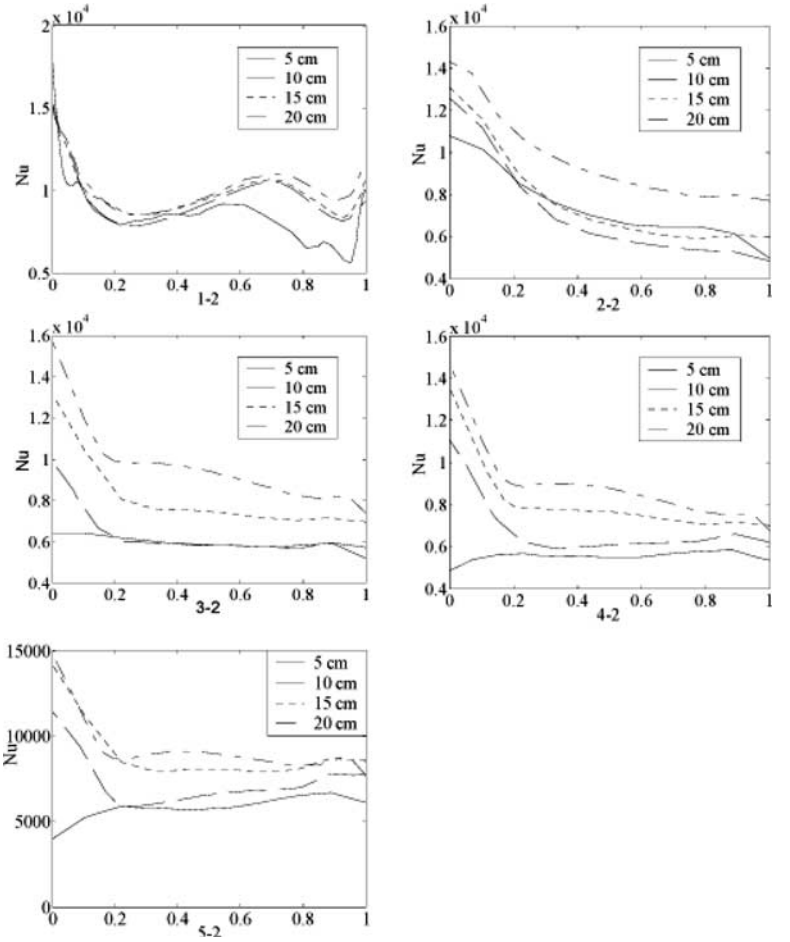

FIG. 6—*The computed Nusselt number (Nu) variation over the top surface of each disk, for all interdisk spacings. The abscissas are the dimensionless coordinate* χ_2. $V_i = 20\ m/s$ $(Re = 6.54 \times 10^6)$.

models which describe the flow details in a better way, it is good for starting the analysis of these complex flows, because it is relatively efficient for computations and because there is much experience with its use. We note that the flow was assumed to be steady. Vortex shedding effects may be interesting to examine in a more fundamental study of such flows, which would require much more rigorous modeling of the turbulent flow, perhaps using direct numerical simulation or large eddy simulation, but these type of models are extremely time consuming even for low Reynolds number flows, let alone for the considered practical quenching high Reynolds numbers. An approximate evaluation of the vortex shedding in such flows impinging on circular disks shows that its frequency is about 40 s^{-1} to 400 s^{-1}, high enough to be unlikely to affect average heat transfer during quenching time.

The constants used in the model are those recommended by CFX. Of particular importance for good characterization of the flow and heat transfer near the body surfaces is to maintain a near-wall computational grid small enough, and the CFX scalable wall function approach was taken. It allows application of arbitrarily fine meshes without violating the underlying logarithmic velocity profile assumption. It assumes that the surface coincides with the edge of the viscous sublayer, which is defined to be at $y^+ = (u^* \Delta n / 4)/\mu = 11$ (this is typically the distance outside the viscous sublayer but still very close to the wall), and the intersection between the logarithmic and the linear near-wall profile. The computed y^+ is not allowed to fall below this limit and all grid points are outside the viscous sublayer; all fine grid inconsistencies are thus avoided.

The mesh density used for the computation, of 100 000–130 000 nodes was determined by examining grid dependence of the Nu. Halving the mesh size resulted in acceptable differences of up to below 10 %, and typically below 5 %.

Since the velocities considered are a small fraction of the speed of sound, the flow is assumed to be

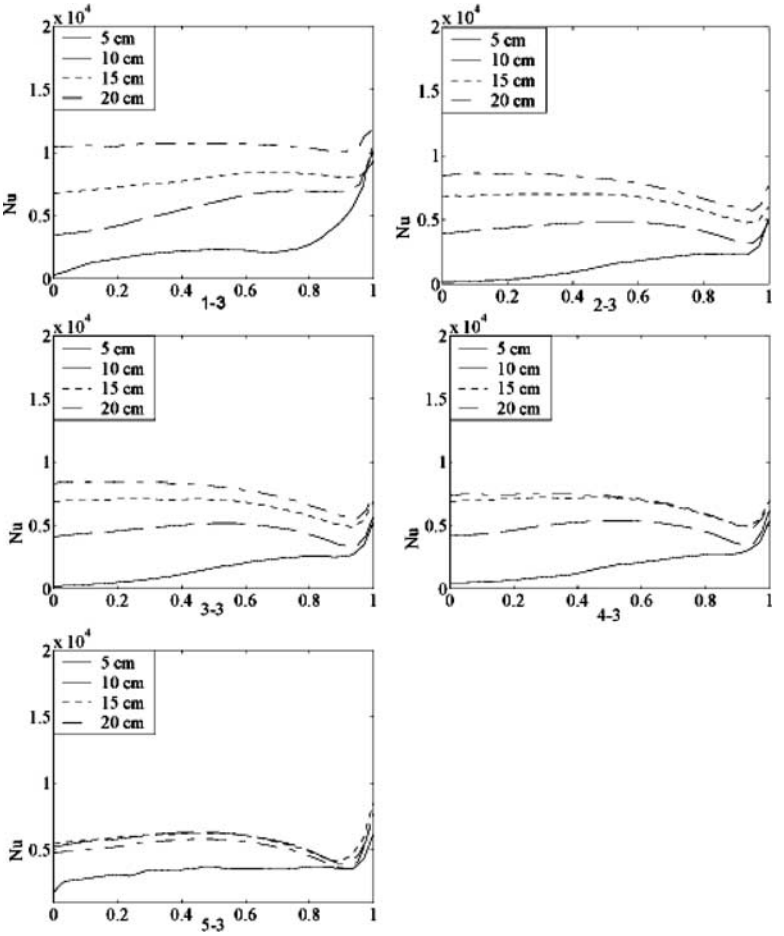

FIG. 7—*The computed Nusselt number (Nu) variation over the back surface of each disk, for all inter-disk spacings. The abscissas are the dimensionless coordinate* χ_3. $V_i = 20\ m/s$ $(Re = 6.54 \times 10^6)$.

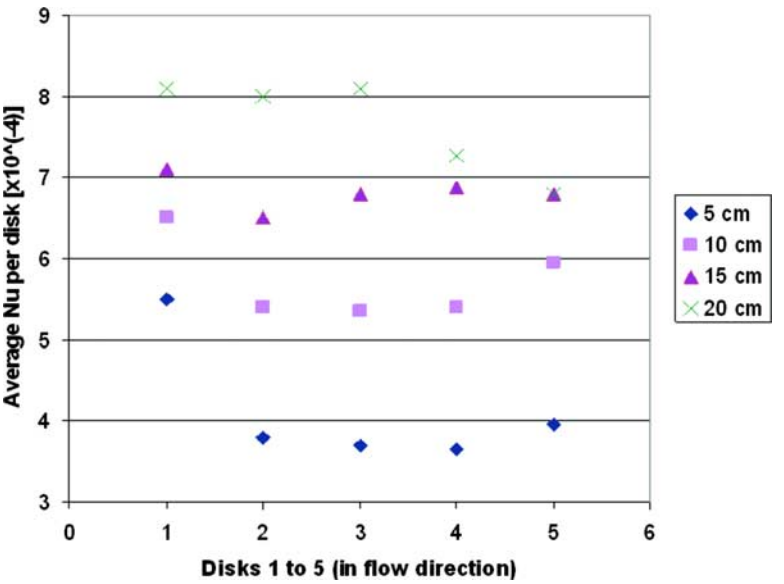

FIG. 8—*Area-averaged Nusselt number,* $\overline{Nu}$, *for all solid disks at all interdisk spacings.* $V_i = 20\ m/s$ $(Re = 6.54 \times 10^6)$.

TABLE 2—*Heat transfer results for each solid disk at all interdisk spacings a; in the last column, the numbers 1, 2, 3, and 4 correspond to a = 5, 10, 15, and 20 cm, respectively. The disks are numbered 1 to 5 in the flow direction, 1 being the most upstream one.* $V_i = 20$ *m/s* ($Re = 6.54 \times 10^6$).

Disk number	a, cm	σ_{Nu}	$\bar{Nu}$	Nu_{max}/Nu_{min}	Range $Nu_{,min}$ to $Nu_{,max}$	Spacing order Nu_{max} to Nu_{min}
1	5	0.48	5772	78.9	307–24 236	4
	10	0.33	6726	38.5	893–34 425	2
	15	0.30	7378	39.2	881–34 511	1
	20	0.25	8394	37.0	890–32 958	3
2	5	0.51	3940	83.7	143–11 969	4
	10	0.34	5597	5.87	2724–15 981	1
	15	0.28	6693	4.36	3264–14 247	3
	20	0.22	8210	3.69	4165–15 355	2
3	5	0.33	3714	47.5	151–7 177	4
	10	0.28	5371	4.24	3133–13 276	3
	15	0.27	7053	3.61	4845–17 507	1
	20	0.27	8338	4.41	3888–17 133	2
4	5	0.26	3550	39.3	173–6 795	4
	10	0.29	5577	6.69	2116–14 152	3
	15	0.27	7057	4.91	3207–15 743	2
	20	0.28	7600	5.28	3458–18 270	1
5	5	0.19	4022	31.4	243–7 622	4
	10	0.29	6072	7.89	2346–18 495	3
	15	0.29	7051	5.96	3214–19 160	2
	20	0.31	6986	7.36	2983–21 958	1

TABLE 3—*The overall pressure difference between the computational domain inlet and exit, with the five solid disks in it, for all interdisk spacing a.* $V_i = 20$ *m/s* ($Re = 6.54 \times 10^6$).

a, cm	Flow domain length, m	Overall pressure difference, Pa
5	1.50	261.9
10	1.75	305.8
15	2.00	363.2
20	2.25	415.8

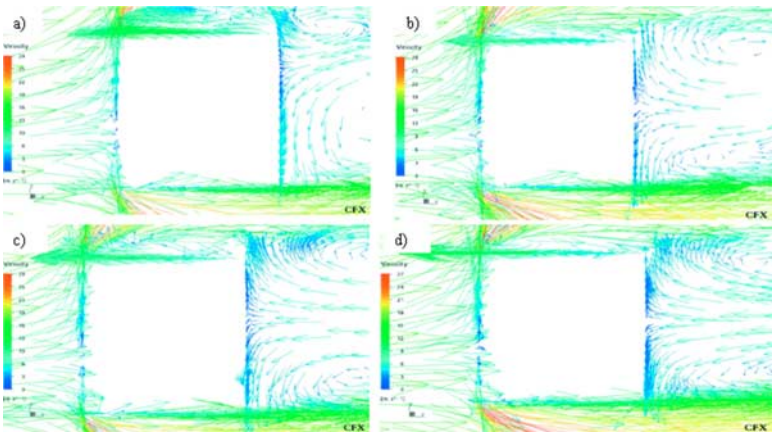

FIG. 9—*The computed velocity field for disk 1 with hole at interdisk spacings (a) of (a) 0.05 m, (b) 0.10 m, (c) 0.15 m, and (d) 0.20 m. Each rectangle represents the cross section of the solid part of the disk, and the hole is at the bottom of each rectangle. The flow is from left to right.* $V_i = 20$ *m/s* ($Re = 6.54 \times 10^6$).

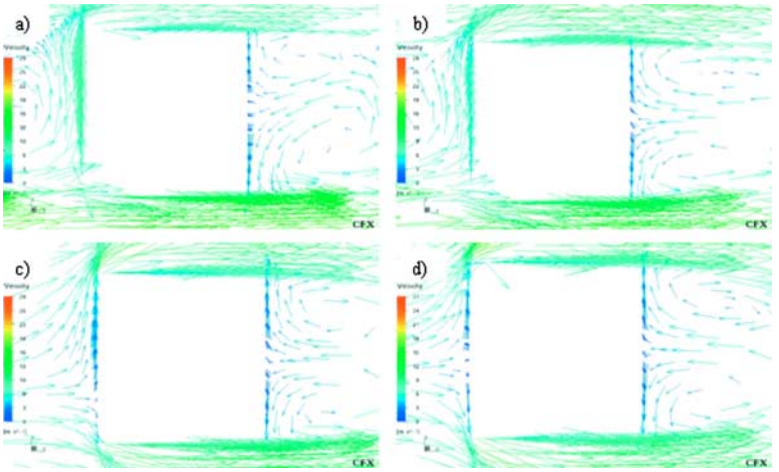

FIG. 10—*The computed velocity field for disk 3 with hole at interdisk spacings (a) of (a) 0.05 m, (b) 0.10 m, (c) 0.15 m, and (d) 0.20 m. Each rectangle represents the cross section of the solid part of the disk, and the hole is at the bottom of each rectangle. The flow is from left to right.* $V_i = 20$ *m/s (Re* $= 6.54 \times 10^6$*).*

incompressible. The turbulence intensity I is defined as $I = v/V_i$, where v is the turbulent fluctuation velocity and V the inlet velocity, and was kept at 3.7 %.

In the computation, the disks are held isothermal at 900°C. Full axial symmetry is assumed, and to save computation time only 1/8 of the cross-sectional domain is computed.

An attempt was made to validate the model against available experimental data from the literature, but no data appropriate for comparison were found. Successful verification of at least the general correctness of the pressure drop is shown in the Results section ("Solid Disks") below.

The heat transfer coefficients were defined by Nusselt numbers, where in general

$$\mathrm{Nu} \equiv \frac{hd_o}{k} \tag{1}$$

where h is the surface convective heat transfer coefficient, d_o the disk outer diameter, and k the gas (N_2) thermal conductivity at 293 K, 20 bar. $\mathrm{Nu_{min}}$ and $\mathrm{Nu_{max}}$ are its minimal and maximal values on each disk surface, respectively. We also show for each disk the surface-averaged Nusselt number $\bar{\mathrm{Nu}}$, as well as the

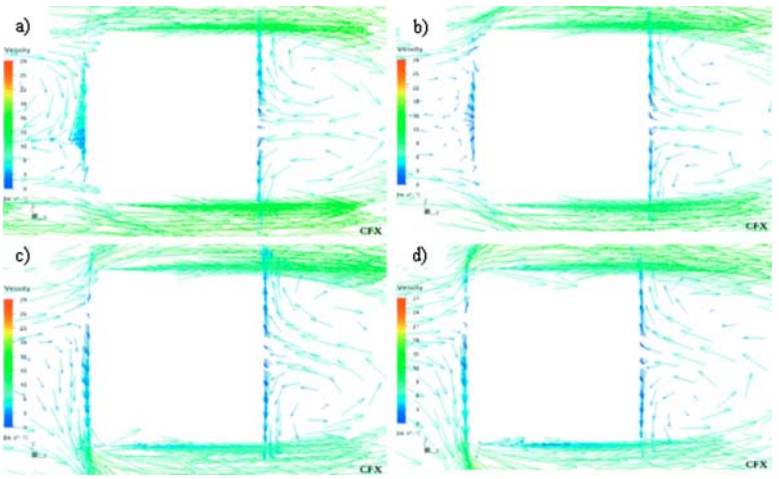

FIG. 11—*The computed velocity field for disk 5 with hole at interdisk spacings (a) of (a) 0.05 m, (b) 0.10 m, (c) 0.15 m, and (d) 0.20 m. Each rectangle represents the cross section of the solid part of the disk, and the hole is at the bottom of each rectangle. The flow is from left to right.* $V_i = 20$ *m/s (Re* $= 6.54 \times 10^6$*).*

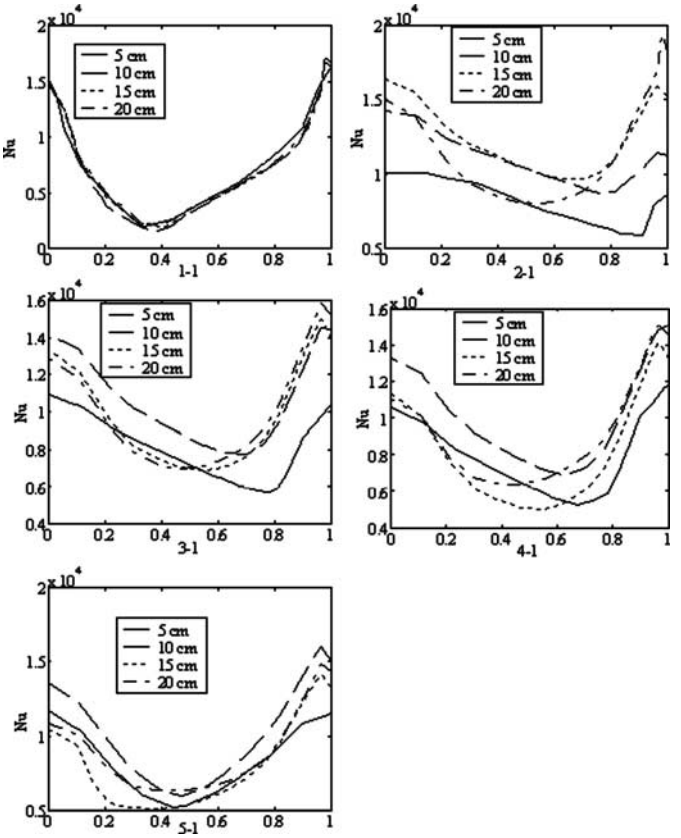

FIG. 12—*The computed Nusselt number (Nu) variation over the frontal surface of each disk with hole, for all interdisk spacings. The abscissas are the dimensionless coordinate* χ_1. $V_i = 20\ m/s$ $(Re = 6.54 \times 10^6)$.

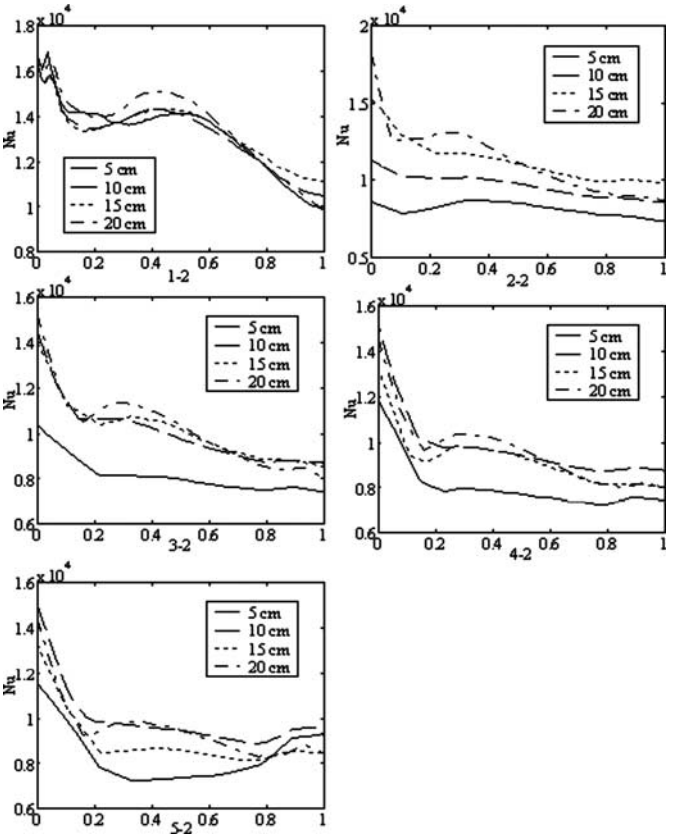

FIG. 13—*The computed Nusselt number (Nu) variation over the top surface of each disk with hole, for all interdisk spacings. The abscissas are the dimensionless coordinate* χ_2. $V_i = 20\ m/s$ $(Re = 6.54 \times 10^6)$.

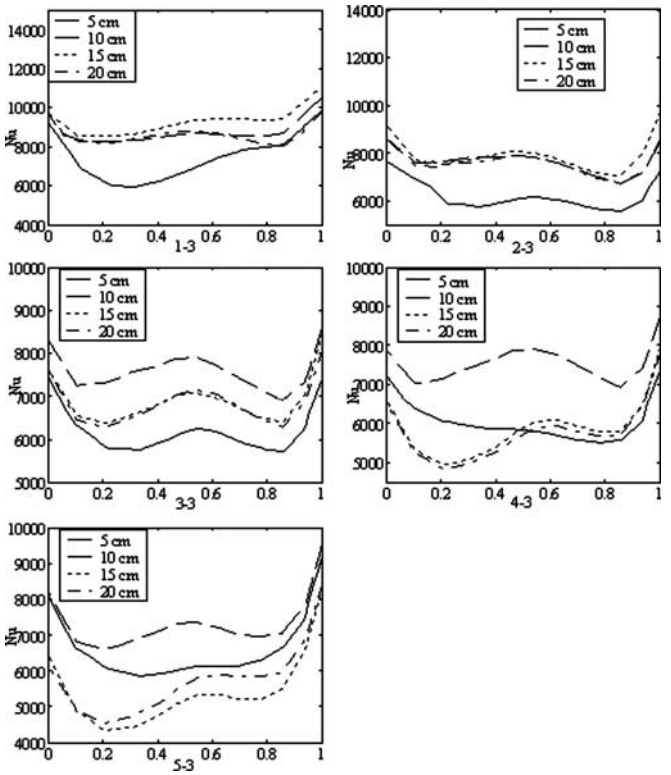

FIG. 14—*The computed Nusselt number (Nu) variation over the back surface of each disk with hole, for all interdisk spacings. The abscissas are the dimensionless coordinate* χ_3. $V_i = 20$ *m/s* ($Re = 6.54 \times 10^6$).

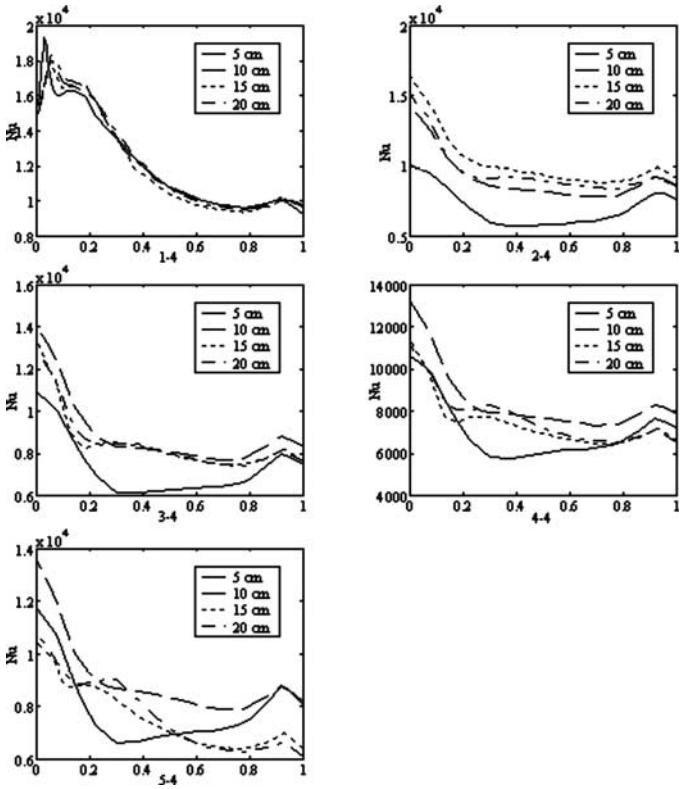

FIG. 15—*The computed Nusselt number (Nu) variation over the inside surface of each disk with hole, for all inter-disk spacings. The abscissas are the dimensionless coordinate* χ_4. $V_i = 20$ *m/s* ($Re = 6.54 \times 10^6$).

TABLE 4—*The overall pressure difference between the computational domain inlet and exit, with the five disks with holes in it, for all interdisk spacing a.* $V_i = 20$ *m/s* ($Re = 6.54 \times 10^6$).

a, cm	Flow domain length, m	Overall pressure difference, Pa
5	1.50	247.9
10	1.75	313.5
15	2.00	371.1
20	2.25	417.5

Nusselt number "relative standard deviation" nonuniformity σ_{Nu} for total disk area A_t, including the flat ends and the envelope, defined as

$$\sigma_{Nu} \equiv \frac{\frac{1}{A_t}\{\int_{A_t}[(Nu - \overline{Nu})dA]^2\}^{1/2}}{\overline{Nu}} \tag{2}$$

where Nu is the local Nusselt number at surface area element dA.

Results

General

Figures 2 and 3 serve to identify the disks and their surfaces.

Solid Disks

Figure 4 shows the entire computed velocity field for the smallest and the largest distance between the disks. The typical flow configuration, starting from the upstream disk, is (i) stagnation flow on the upstream surface, accelerating from the center towards the disk corner, (ii) separation at the corner and change of direction to axial flow, (iii) fast flow over all the disks' circumferences (surface 2, Fig. 3), (iv) much slower circulation type flows between the disks, decreasing in the radial direction, and in the wake of the downstream one, and (v) some increase of the velocity between the disks with their interdisk spacing *a*.

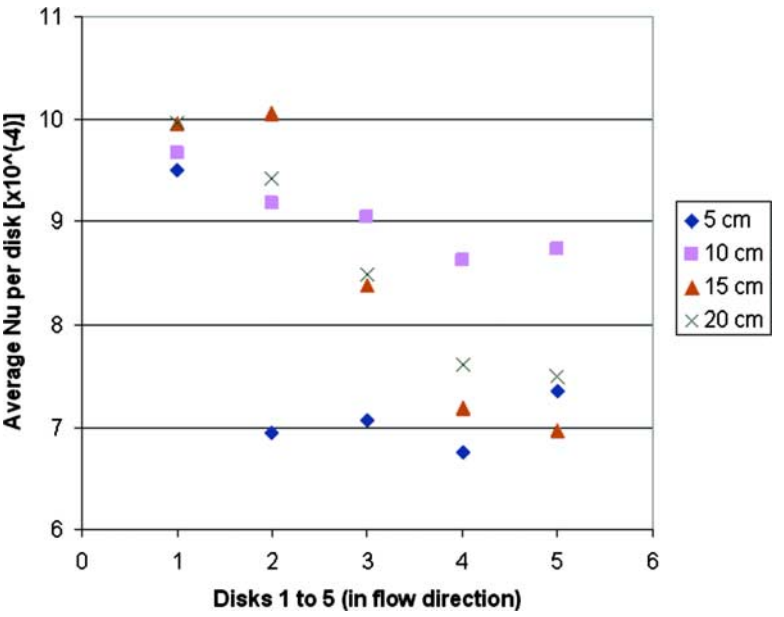

FIG. 16—*Area-averaged Nusselt number* $\overline{Nu}$ *for disks with holes at all interdisk spacings.* $V_i = 20$ *m/s* ($Re = 6.54 \times 10^6$).

TABLE 5—*Heat transfer results for each disk with hole at all interdisk spacings a; in the last column, the numbers 1, 2, 3, and 4 correspond to a = 5, 10, 15, and 20 cm, respectively. The disks are numbered 1 to 5 in the flow direction, 1 being the most upstream one.* $V_i = 20$ *m/s* ($Re = 6.54 \times 10^6$).

Disk number	a, cm	σ_{Nu}	$\bar{Nu}$	Nu_{max}/Nu_{min}	Range $Nu_{,min}$ to $Nu_{,max}$	Spacing order Nu_{max} to Nu_{min}
1	5	0.28	9289	50.8	732–37 215	4
	10	0.26	10044	52.7	711–37 451	3
	15	0.25	10320	57.8	648–37 452	2
	20	0.27	10312	56.0	686–38 391	1
2	5	0.16	7204	4.14	4991–20 655	4
	10	0.15	9423	3.18	6705–21 329	2
	15	0.17	10378	3.07	6866–21 050	3
	20	0.22	9742	4.71	6635–31 259	1
3	5	0.19	7291	3.79	5095–19 300	4
	10	0.19	9293	3.36	6724–22 585	3
	15	0.22	8638	4.77	5387–25 698	2
	20	0.22	8741	4.61	5983–27 561	1
4	5	0.23	7061	4.15	4623–19 186	3
	10	0.20	8887	2.90	6626–19 186	3
	15	0.25	7454	4.97	4609–22 900	2
	20	0.23	7898	5.66	4464–25 281	1
5	5	0.24	7583	5.24	3929–20 574	4
	10	0.23	8945	4.30	5154–22 167	3
	15	0.25	7217	6.07	3681–22 341	2
	20	0.23	7774	6.06	4286–25 978	1

Figures 5–7 show the variation of Nu for each disk surface for all disk spacings. Figure 5 shows that for the upstream (front) surface of all the disks (surface *X*-1): (i) Nu increase from a minimum at $r=0$ to a maximum at $r=d_o/2$; The justification of this behavior can be seen from an examination of the velocity fields (Fig. 4), which shows acceleration for the front surface of all disks, boundary layer thinning, and increased turbulation of the flow from the center to the outer corner, which of course is most obvious for the upstream disk, and (ii) Nu at this surface of the downstream disks increases with the interdisk spacing (a) because the velocities between the disks increase with a.

Comparing Nu at surface *X*-2 (the circumference, or "top") for all spacings (Fig. 6) shows that Nu first drops rapidly from a maximum at $\chi_2=0$ until about $\chi_2 \sim 0.2$. At the first disk (1-2), Nu has a minimum at $\chi_2 \sim 0.2$, and it rises for all spacings except 5 cm to a maximum at about 0.70–0.75, proceeds to drop to a second minimum at about 0.95, and then rises to a third maximum at $\chi_2=1$. For the 5 cm spacing the maximum is attained already at $\chi_2 \sim 0.55$. At the second disk (surface 2-2), Nu continues dropping to a minimum at $\chi_2=1.0$. At surfaces 3-2, 4-2, and 5-2, Nu for all spacings except 5 cm drops to a relatively steady value, while for the 5 cm case it remains approximately constant over *X*-2 at a value between 5000 and 11 000. Similar to the explanation of the behavior at surfaces *X*-1, this behavior can be explained by observing the velocity plots in Fig. 4, where high values of Nu arise from high velocity gradients (thinning of boundary layers) and turbulence due to flow separations.

As expected, the Nu change similarly for all spacings for the back side (*X*-3) of each disk (Fig. 7). For disks 2 to 4, the curves follow the same pattern and the Nu levels are about the same. In general, Nu is most uniform on these surfaces. Due to the low velocities at the rear surfaces (3) of the disks (Fig. 4), Nu there is relatively low (Fig. 7), and becomes lower as the spacing decreases. It is fairly uniform along the surfaces, reaching a local maximum near the corner (for $\chi_3 > 0.9$) due to flow separation, followed by an increase at the corner due to the higher turbulence there.

Figure 8 shows the area-averaged Nu: $\overline{Nu}$. For the upstream disk, 1, $\overline{Nu}$ is the highest and then becomes lower and uniform for disks 2 to 5. The differences between disk 1 and the others become smaller as the spacing between the disks is increased.

Table 2 summarizes the Nu, σ_{Nu}, and $\overline{Nu}$ values, ranges, and ratios for each surface and spacing, allowing easy estimation of heat transfer coefficient magnitudes and nonuniformities. One clear conclusion

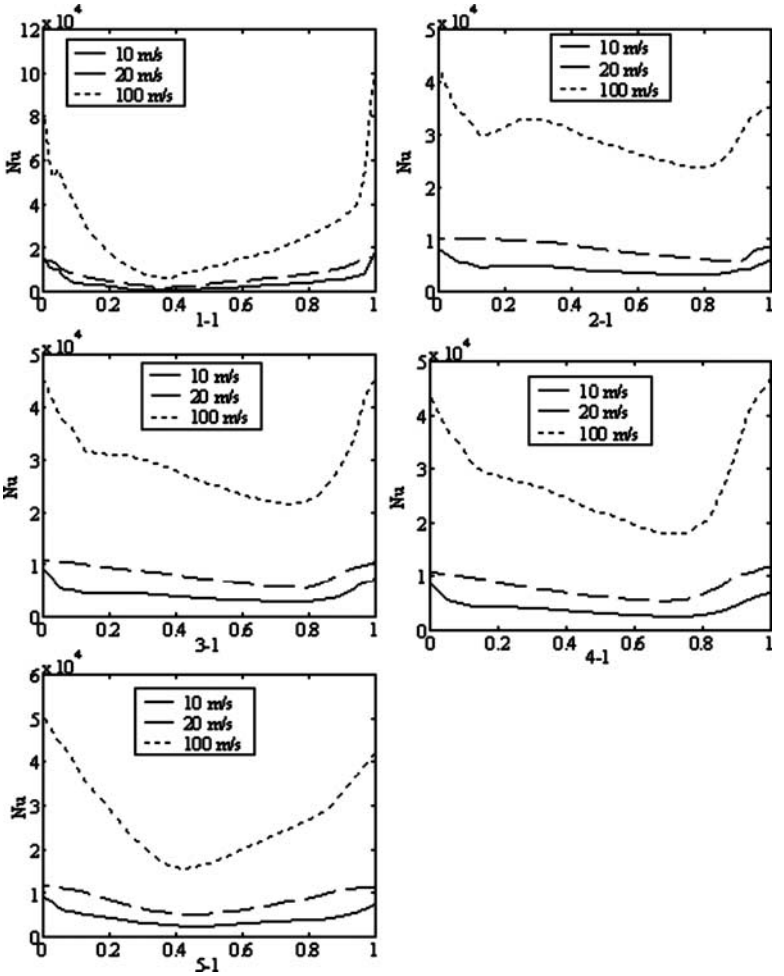

FIG. 17—*The computed Nusselt number (Nu) variation over the frontal surface of each disk with hole, for* $a = 0.05$ *m, for* $V_i = 10$, *20, and 100 m/s (*$Re = 3.27 \times 10^6$, 6.54×10^6, 32.7×10^6, *respectively). The abscissas are the dimensionless coordinate* χ_1.

is that uniformity improves as the spacing is increased, but in an asymptotic way, gaining most improvement up to a spacing of about 10 cm. Another conclusion is that $\overline{\text{Nu}}$ is much higher for the most upstream disk (1) and remains relatively the same for the downstream disks.

The overall pressure drop, that is the difference between the inlet and exit of the domain, is shown in Table 3. It is shown to increase with the interdisk spacing, rising by about 60 % as the spacing is increased from 5 cm to 20 cm. As a partial attempt to validate the results, experimental results from [15], available only for a single round disk, were used and predicted a pressure drop of 266 Pa, very close to our multidisk results shown in the table. Our computations show slightly higher values, consistent with the experimental observations [15,16] that two disks in tandem would have a higher pressure drop than a single one.

Disks with a Concentric Hole

A similar analysis was performed for the axially aligned disks having a concentric hole (Fig. 1(*b*)). Figures 9–11 show the flow fields for the first, third, and fifth disks (counting in the downstream direction), respectively. Figures 12–15 show the Nusselt number distributions along the front, top, back, and inside surfaces, respectively, for all interdisk spacings and for each disk.

Nu for the front (*X*-1) and rear (*X*-3) surfaces of all cylinders exhibits a minimum between maxima at the corners, reflecting well the behavior shown in the velocity field Figs. 9–11. On both surfaces, the flow is of the impinging type, with stagnation between the corners, and acceleration as they are approached.

The behavior at the top surface (*X*-2) is similar to that for cylinders without holes, as discussed before.

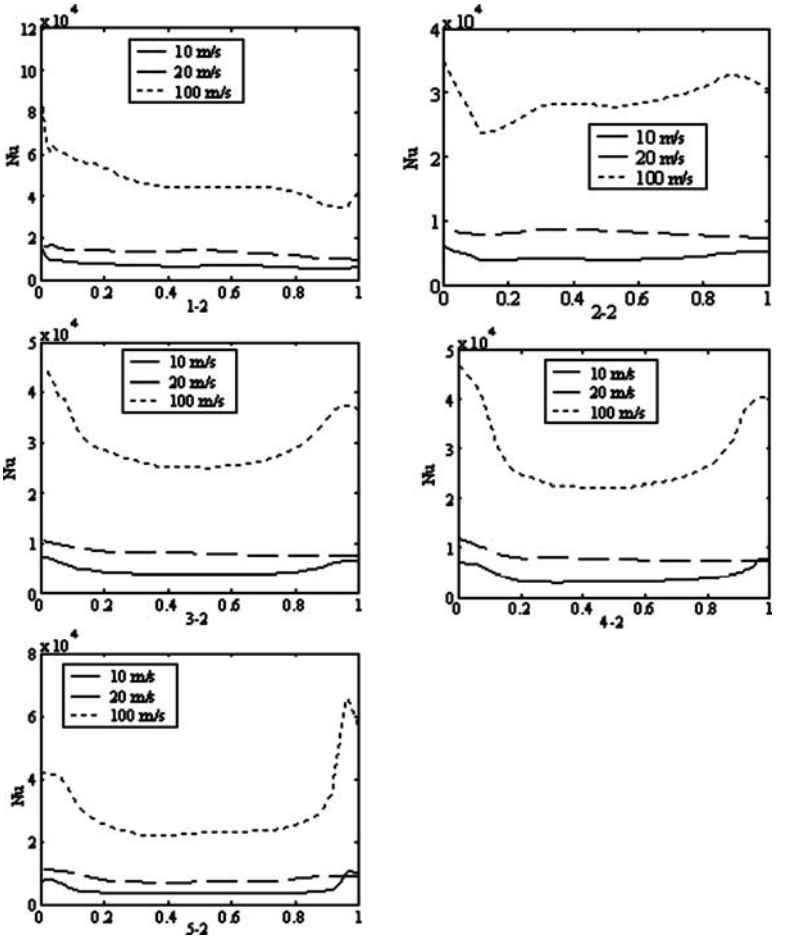

FIG. 18—*The computed Nusselt number (Nu) variation over the top surface of each disk with hole, for* $a = 0.05$ *m, for* $V_i = 10$, *20, and 100 m/s (*$Re = 3.27 \times 10^6$, 6.54×10^6, 32.7×10^6, *respectively). The abscissas are the dimensionless coordinate* χ_2.

The small local maxima occurring for χ_2 between 0.2 and 0.4 are due to the backflow reattachment. The only difference one can see is in 5-2 for the 5 cm case, where Nu rises towards the upper corner because no solid bodies are present downstream.

For the back surfaces (X-3), it is noteworthy that the most efficient cooling on surface 1-3 is for $a = 15$ cm—not by much, though. Nu has a dip of 10 % to 75 % only for $a = 5$ cm. For larger values of a, it follows the same trend as the others.

As expected, Nu values follow each other independently of a, just like on the frontal area. The highest cooling is from the beginning of the surface, $\chi_3 = 0$, until χ_3 reaches 1/5 of the length. In general, less cooling is obtained for $a = 5$ cm due to the tighter geometry, whereas fairly equal values of Nu are obtained for the other interdisk spacings.

Inside the hole, surface X-4, Nu is seen to decrease along χ_4, as expected based on the velocity field Figs. 9–11, characteristic of boundary layer growth, with Nu augmented at the front corner due to the increased turbulence there, and then in some cases also augmented somewhat near the rear corner due to the confluence with the backflow.

The overall pressure drops, shown in Table 4, are in the same range as for the solid disk, and also increasing by 60 % as a is increased from 5 cm to 20 cm.

The primary results are summarized in Fig. 16 and Table 5. Understandably, the heat transfer coefficients are higher for the disks with holes, because, as demonstrated in Figs. 9–11, the velocities along the disk surfaces are higher, and holes add steps and turbulence in the flow field. Interestingly, the augmentation of the flow through the hole creates the highest $\overline{\mathrm{Nu}}$ at disk 2, instead of at disk 1 when the disks were solid. Also differing from the case of solid disks, the maximal $\overline{\mathrm{Nu}}$ for disks 2 to 5 occurs for $a = 10$ cm. This can be explained by the confluence of the flows through the holes and above the circumference, which produce higher cooling already at smaller spacings.

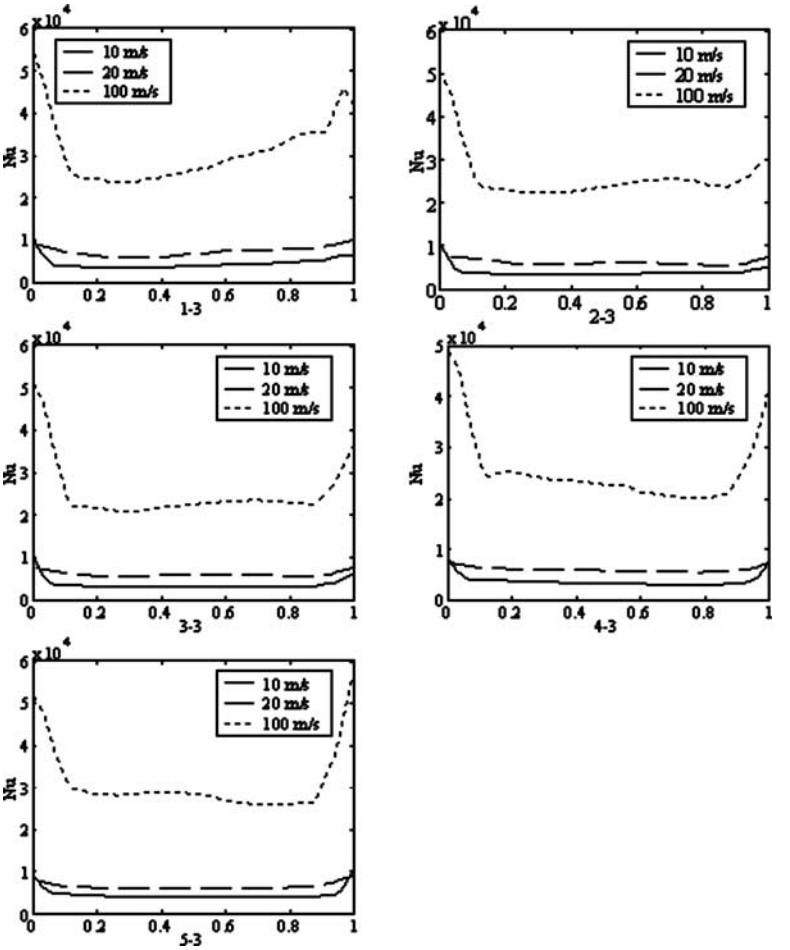

FIG. 19—*The computed Nusselt number (Nu) variation over the frontal surface of each disk with hole, for* $a = 0.05$ *m, for* $V_i = 10$, *20, and 100 m/s (*$Re = 3.27 \times 10^6$, 6.54×10^6, 32.7×10^6, *respectively). The abscissas are the dimensionless coordinate* χ_3.

To examine the effect of the approach flow velocity V_i on the disks with hole, computations of the flow fields and of Nu were made for $V_i = 10$, 20, and 100 m/s for a = 5 cm, and Figs. 17–20 show the Nusselt number distributions along the front, top, back, and inside surfaces, respectively, for each disk. The Nu peaks at the corners are partially due to higher velocities, but another influence may be the weakness of the turbulence model to compute correctly at corners.

The heat transfer patterns are similar, with approximately $\overline{\mathrm{Nu}} \propto \mathrm{Re}^{0.85}$ for both the solid and holed disks.

The overall pressure drops for the three velocities are shown in Table 6, and confirm dependence on V_i^2. Comparing Table 3 with Table 6, we clearly can see that the velocity has a stronger effect on the pressure drop than the interdisk spacing.

Figure 21 shows the $\overline{\mathrm{Nu}}$ for all disks at the three approach velocities. For each velocity, $\overline{\mathrm{Nu}}$ for disks 2 to 5 is roughly the same, while that for disk 1 is higher by magnitudes that increase with the velocity. $\overline{\mathrm{Nu}}$ rises with the velocity: compared with its value for 10 m/s, it is twice as large for 20 m/s and almost seven times higher for 100 m/s. Table 7 summarizes the results for the effects of the approach velocity V_i on heat transfer.

Conclusions

The numerical analysis shows that in axial flow cooling of short disks, the heat transfer coefficients along the disk surfaces vary strongly up to a worse case of two orders of magnitude for the upstream disk. This nonuniformity is much lower for the disks downstream of the first one, indicating that in quenching application, the first disk should just be there for flow presence but not for being quenched. For the disks

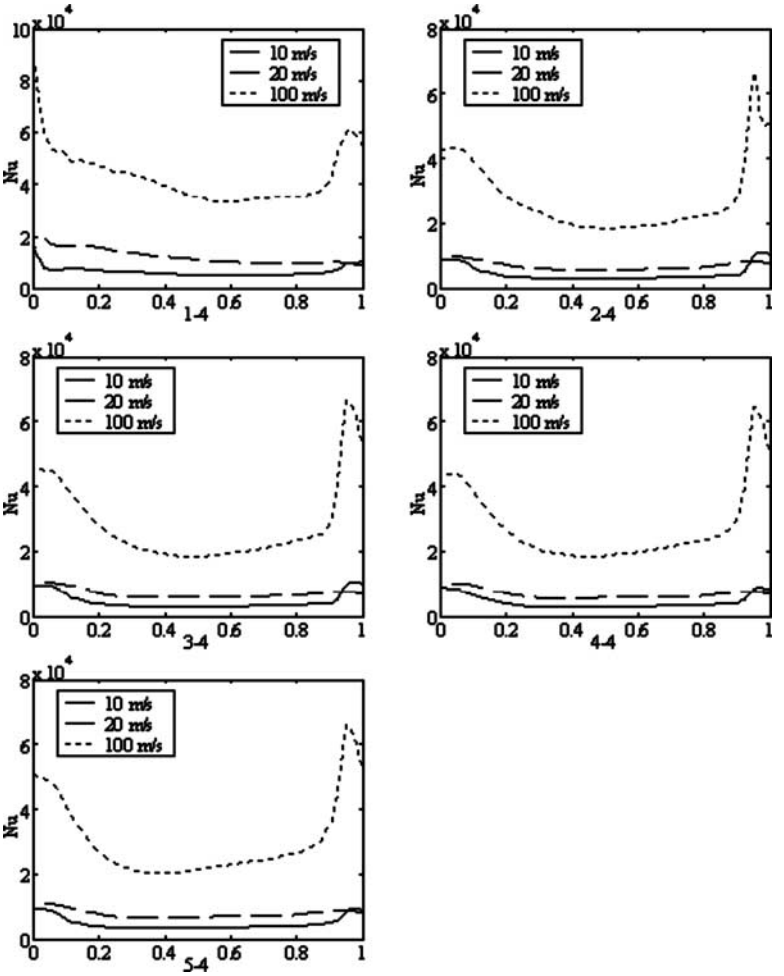

FIG. 20—*The computed Nusselt number (Nu) variation over the inside surface of each disk with hole, for* $a = 0.05$ *m, for* $V_i = 10$*, 20, and 100 m/s (*$Re = 3.27 \times 10^6$*,* 6.54×10^6*,* 32.7×10^6*, respectively). The abscissas are the dimensionless coordinate* χ_4*.*

with a concentric hole, uniformity is attained for the disks after the second. Increasing the spacing between the disks to 10 cm or more also has an important effect on improving cooling uniformity. Even with this remedy, the Nusselt number ratios along surfaces are of the order of 5, indicating that quenching of multiple, disks in such axial flows may not be optimal for bodies which are sensitive to cooling nonuniformity. At the same time, is important to note that the temperature variation in the solid is likely to be much smaller; a recent study with jet impingement cooling of various steels [17] has shown that it was in that particular case an order of magnitude smaller than the variation in the surface heat transfer coefficient. The overall pressure drop along the flow increases with the interdisk spacing, rising by about 60 % as the spacing is increased from 5 cm to 20 cm. V_i was found to affect the magnitude of heat transfer, approximately as $\overline{\mathrm{Nu}} \propto \mathrm{Re}^{0.85}$ as well as of the pressure drop approximately as Re^2, but not the general flow and heat transfer dsitribution patterns.

TABLE 6—*The overall pressure difference between the computational domain inlet and exit, with the five disks with holes in it, for* $V_i = 10$*, 20, and 100 m/s (*$Re = 3.27 \times 10^6$*,* 6.54×10^6*,* 32.7×10^6*, respectively).* $a = 5$ *cm.*

V_i, m/s	Overall pressure difference, Pa
10	64.2
20	247.9
100	6008.8

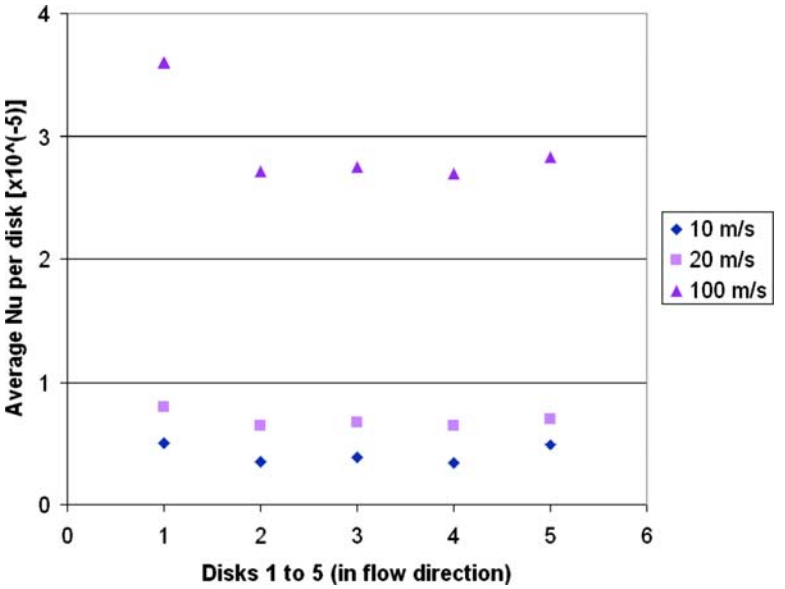

FIG. 21—*Area-averaged Nusselt number* $\overline{Nu}$ *for disks with holes for* $a = 0.05$ *m, for* $V_i = 10$, *20, and 100 m/s (*$Re = 3.27 \times 10^6$, 6.54×10^6, 32.7×10^6, *respectively).*

TABLE 7—*Heat transfer results for each disk with hole for* $V_i = 10$, *20, and 100 m/s (*$Re = 3.27 \times 10^6$, 6.54×10^6, 32.7×10^6, *respectively). In the last column the numbers 1, 2, and 3 correspond to* $V_i = 10$, *20, and 100 m/s, respectively. The disks are numbered 1 to 5 in the flow direction, 1 being the most upstream one.* $a = 0.05$ *m.*

Disk number	a, cm	σ_{Nu}	$\bar{Nu}$	Nu_{max}/Nu_{min}	Range $Nu_{,min}$ to $Nu_{,max}$	Order of V_i Nu_{max} to Nu_{min}
1	10	0.29	5554	48.7	413–20 114	3
	20	0.28	9289	50.8	732–37 215	2
	100	0.24	37573	23.9	4683–111 897	1
2	10	0.15	4077	3.64	3027–11 013	3
	20	0.16	7204	4.14	4991–20 655	2
	100	0.14	27874	4.17	18341–76 519	1
3	10	0.19	4125	3.66	2909–10 635	3
	20	0.19	7291	3.79	5095–19 300	2
	100	0.17	28225	4.34	16704–73 266	1
4	10	0.22	4024	3.69	2427–8 939	3
	20	0.23	7061	4.15	4623–19 186	2
	100	0.22	27326	4.18	16704–69 891	1
5	10	0.23	4348	4.76	2297–10 939	3
	20	0.24	7583	5.24	3929–20 574	2
	100	0.23	29002	4.43	15637–69 319	1

Acknowledgments

This study was performed mostly at the Faxénlaboratoriet of the Kungl. Tekniska Högskolan (KTH), Stockholm, and primarily sponsored by The Swedish Institute of Production Engineering Research (IVF) under project AIS23 "Gas Quenching for Environmentally Sound Quenching," and by LindeGas GmbH (formerly AGA AB), and Ipsen International GmbH. The authors are grateful for the technical assistance of Dr. Michael Vynnycky in this work.

References

[1] Midea, S. J., Holm, T., Segerberg, S., Bodin., J., Thors., T., and Swartström, K., "High Pressure Gas Quenching—Technical and Economic Considerations," *Proc. 2nd Int. Conf. On Quenching and the*

Control of Distortion, ASM International, Materials Park, OH, 1996, p. 157.

[2] Ferrari, J., Ipek, N., Lior, N., and Holm, T., "Gas Quench Vessel Efficiency: Experimental and Computational Analysis," Proc. 18th *ASM International Heat Treating Soc. Conf.*, Rosemont, IL, ASM International, Materials Park, OH, 1998, pp. 500–505.

[3] Ferrari, J., Ipek, N., Lior, N., and Holm, T., "Flow Considerations in Quenching Vessels," *Proc. ASM International International 3rd Conference on Quenching and Control of Distortion*, Prague, Czech Republic, ASM International, Materials Park, OH, 1999, pp. 93–101.

[4] Lind, M., Lior, N., Alavyoon, F., and Bark, F., "Flows Effects and Modeling in Gas-Cooled Quenching," *Proc. Heat Transfer 1998, 11th International Heat Transfer Conference*, Korea, Korean Society of Mechanicel Engineers, Seoul, Korea, 1998, Vol. 3, pp. 171–176.

[5] Thuvander, A., Melander, A., Lind, M., Lior, N., and Bark, F. "Prediction of Convective Heat Transfer Coefficients and Their Effects on Distortion and Mechanical Properties of Cylindrical Steel Bodies Quenched by Gas Cooling," *5th ASME/JSME Joint Thermal Engineering Conference*, March 15–19, 1999, San Diego, ASME, New York, Paper AJTE99-6289.

[6] Thuvander, A., Melander, A., Lind, M., Lior, N., and Bark, F., "Prediction of Convective Heat Transfer Coefficients and Their Effects on Distortion and Mechanical Properties of Cylindrical Tubes Quenched by Gas Cooling," *La Metallurgia Italiana*, Vol. XCI, 4, 1999, pp. 25–32.

[7] Wiberg, R., Muhammad-Klingmann, B., and Ferrari, J., and Lior, N., "Thermochromic Coatings Help Characterize Gas Quenching," *ASM International Heat Treating Progress*, Vol. 158 No. 4, 2000, pp. 37–40.

[8] Ferrari, J., Lior, M., and Slycke, J., "An Evaluation of Gas Quenching of Steel Rings by Multiple-Jet Impingement," *J. Mater. Process. Technol.* Vol. 136, 2003, pp. 190–201.

[9] Vynnycky, M., Ferrari, J., and Lior, N., "Some Analytical And Numerical Solutions to Inverse Problems Applied to Phase-Transformation Tracking Gas Quenching," *J. Heat Transfer* Vol. 125, No. 1, 2003, pp. 1–10.

[10] Lior, N., "The Cooling Process in Gas Quenching," *J. Mater. Process. Technol.*, Vol. 155–156, 2004, pp. 1881–1888.

[11] Tensi, H. M., Stich, A., and Totten, G. E., "Quenching and Quenching Technology," *Steel Heat Treatment Handbook*, Marcel Dekker, New York, 1997, chap. 4, p. 157.

[12] Fritsching, U., and Schmidt, R., "Gas Flow Control in Batch Mode High Pressure Gas Quenching," *Proceedings European Conference on Heat Treatment* Innovation in Heat Treatment for Industrial Competitiveness', Verona 2008, May 7–9, Heat Treatment and Metallography Study Group of Associazione Italiana Di Metallurgia, Piazzale Rodolfo Morandi 2-I-20121 Milano, Italy.

[13] Lior, N., and Papadopoulos, D., "Refroidissement au Gaz de Cylindres Courts Multiples dans un écoulement Axial (Gas-cooling of Multiple Short Cylinders in Axial Flow)," *Proc. ATT/AWT/ASTT-SVW/VWT Journées Européennes-Refroidissement et Trempe*, Strassbourg, France, March 18–19 2004; ATTI Association Technique de Traitement Thermique, Paris, France and Arbeitsgemeinschaft Warmebehandlung und Werkstofftechnik e. V. Bremen, Germany (in French).

[14] CFX5.5.1, http://www.ansys.com/products/cfx.asp.

[15] Eiffel, G., *The Resistance of the Air and Aviation*, Constable & Company Ltd., London and Houghton Mifflin Co., Boston, 1913, p. 65.

[16] Hoerner, S. F., *Fluid-Dynamic Drag*, Published by the author, Nidland Pank, NJ, Library of Congress Card Number 37–13009, 1958.

[17] Zuckerman, N., and Lior, N., "The Relationship Between the Distributions of Slot-Jet-Impingement Convective Heat Transfer and the Temperature in the Cooled Solid Cylinder," *Numer. Heat Transfer*, Vol. 53, No. 12, 2008, pp. 1271—1293.